Experimental Mechanics (2009) 49:91–104
DOI 10.1007/s11340-007-9091-3

Computational Analysis of a Cross-linked Actin-like Network

T. Kim · W. Hwang · R.D. Kamm

Received: 5 May 2007 / Accepted: 10 September 2007 / Published online: 4 October 2007

Abstract Gels formed from G-actin or other filament-forming monomers exhibit a range of morphologies that differ widely in terms of pore size, fiber diameter, degree of isotropy, and frequency of cross-linking or branching. These characteristics are determined, in large part, by the nature and concentration of the proteins that form cross-links between single filaments, yet little is known how filament-forming monomers and cross-linkers assemble to generate a particular network morphology. Some of the important attributes of a cross-linker are the spatial and angular orientation of its two filament binding sites, its size, and stiffness to both rotation and extension. Here, we introduce a Brownian dynamics (BD) simulation model in three dimensions in which actin monomers polymerize and become cross-linked by two types of cross-linking molecules that form either parallel filament bundles or perpendicular cross-links. We analyze the effects of various system parameters on the growth and morphology of the resulting network. Some scaling behaviors emerge that are insensitive to the detailed choice of parameters. Our model thus has the potential as a base BD model that can be further refined for investigating various actin-related phenomena.

Keywords Brownian dynamics · Actin cross-linking proteins · Cytoskeleton · Actin · Computational model

T. Kim
Department of Mechanical Engineering,
Massachusetts Institute of Technology,
Room NE47-313, 77 Massachusetts Avenue,
Cambridge, MA 02139-4307, USA
e-mail: ktyman@mit.edu

W. Hwang
Department of Biomedical Engineering,
Texas A&M University, 3120 TAMU,
College Station, TX 77843-3120, USA
e-mail: hwm@tamu.edu

R.D. Kamm (✉)
Departments of Mechanical Engineering and Biological Engineering, Massachusetts Institute of Technology,
Room NE47-321, 77 Massachusetts Avenue,
Cambridge, MA 02139-4307, USA
e-mail: rdkamm@mit.edu

Introduction

Actin is one of the most abundant proteins in eukaryotic cells and plays a central role in cellular mechanobiology, including such phenomena as migration, structural stability, and numerous intracellular processes [1]. Monomeric actin or G-actin self-assembles into double helical filaments or F-actin, 7~8 nm in diameter and up to several microns in length [2], governed by the processes of nucleation, polymerization, and depolymerization [3]. Three G-actin monomers are believed to be required for nucleation [3, 4], which is followed by elongation via assembly primarily at the plus (barbed) end of the filaments and by shortening via disassembly into G-actin monomers primarily at the minus (pointed) end, in a polarized fashion [1].

Actin filaments (F-actin) assemble into stable networks and bundles that are highly dynamic, generating contractile force during cell migration in conjunction with motor proteins from the myosin family, and the filaments are coupled to membrane proteins that are critical in the response of cells to external stress [5]. Assembly of filaments is mediated by actin cross-linking proteins (ACP) such as α-actinin, fascin, fimbrin, and filamin [2, 6]. Their functional, structural diversity and wide variations among different organisms [7] indicate that

ACPs, together with actin, evolved to meet various mechanical needs of the cell.

The structural arrangement of actin binding sites in ACPs is a major determinant of the organization of F-actin [2]. If the binding sites are aligned in tandem, as is true for fimbrin and fascin, ACPs tend to pack actin filaments into stress fibers as are prevalent in the extension and adhesion of cells. In contrast, ACPs such as filamin, have relatively long, flexible arms and tend to align the filaments into a largely orthogonal network found, e.g., in cortical regions near a plasma membrane. Consequently, the unique characteristics of ACPs determine the spacing and orientation between filaments.

This study is motivated by a desire to understand the structure of an actin network (or a network consisting of similarly organized monomers) based on a minimal set of factors such as nucleation and elongation rate constants, G-actin concentrations, ACP type, and mechanical characteristics of component structures. An ability to predict network morphology based on these parameter values has the potential to provide new insight into various biological processes (e.g. cell stiffness, migration, and cytoskeletal morphology). Although we base the model on parameter values that, to the extent possible, correspond to actin monomers and filaments, our primary objective is to study the factors that influence the properties of generic "actin-like" networks. Therefore, simplifications are introduced wherever appropriate to reduce computational cost, while retaining essential features of a 3D polymerized network.

Actin-related phenomena have been extensively modeled. The mechanics of a single actin filament has been studied using molecular dynamics and coarse-grained models [8, 9]. Actin polymerization has been simulated through the combination of free energy calculations, atomically detailed models, and Brownian dynamics (BD) [3, 10] and by analytic theory and stochastic-growth simulation [11]. Others have studied actin filament bundling computationally using an Ising-like mean-field model [12], BD [13], and normal-mode approximations [7]. In addition, actin-powered filopodial extension has been quantified, using Monte Carlo simulation that incorporates F-actin bundles and membranes [14], and the dynamics of membranes driven by the extension including membrane proteins and molecular motors has been also investigated [15, 16]. Nevertheless, a computational investigation of the actin network morphology has not yet been considered.

Here, we simulate polymerization of actin monomers and filament cross-linking by ACPs for a wide range of parameter values. The effects on resultant structures of varying each parameter including nucleation rate constant, initial concentration of actin monomers (C_A), ratio of ACP concentration (C_{ACP}) to C_A (R), orientation of ACP binding sites, bending stiffness of filaments, and size of ACPs are each examined. Their effects are interpreted in terms of influences on filament length, distance between active ACPs, matrix connectivity, polymerization time, mean cross-linking angle, and pore size.

Materials and Methods

In our BD simulation, actin monomers, filaments, and ACPs undergo thermal motion and interact via defined binding probabilities. After the network is formed, morphological properties of the network are examined.

Equations of Motion

The underlying equation for BD, the Langevin equation [17]:

$$m_i \frac{\mathrm{d}^2 \mathbf{r}_i}{\mathrm{d}t^2} = \mathbf{F}_i - \zeta_i \frac{\mathrm{d}\mathbf{r}_i}{\mathrm{d}t} + \mathbf{F}_i^{\mathrm{B}} \tag{1}$$

is employed, where m_i is the mass of the ith molecule (actin monomer or ACP), ζ_i is a friction coefficient, $\mathbf{r}_i$ is the molecule's position, and t is time. $\mathbf{F}_i$ is a net deterministic force as described below, and $\mathbf{F}_i^{\mathrm{B}}$ is a stochastic force having zero average and correlations $\left\langle \mathbf{F}_i^{\mathbf{B}}(t)\mathbf{F}_i^{\mathbf{B}}(t)\right\rangle = \frac{2k_{\mathrm{B}}T\zeta_i\delta_{ij}}{\Delta t}\boldsymbol{\delta}$ [18], where k_{B} is the Boltzmann constant, T is temperature, δ_{ij} is the Kronecker delta, $\boldsymbol{\delta}$ is a unit second-order tensor, and Δt is the simulation time step. The friction coefficient of a molecule, ζ_i, can be expressed as a function of molecular diameter σ_i and medium viscosity η, $\zeta_i = 3\pi\eta\sigma_i$ [19].

Equation (1) is cast in dimensionless form using $k_{\mathrm{B}}T$, ζ_{A}, and σ_{A} (diameter of actin monomers) as primary variables, and dimensionless variables are identified by the tilde "~". Recognizing that inertia is negligible on the length scale of interest, equation (1) takes the simplified dimensionless form:

$$\frac{\mathrm{d}\widetilde{\mathbf{r}}_i}{\mathrm{d}\widetilde{t}} = \left(\widetilde{\mathbf{F}}_i^{\mathrm{B}} + \widetilde{\mathbf{F}}_i\right) \tag{2}$$

For numerical simulations, explicit Euler integration is used to update the locations of molecules:

$$\widetilde{\mathbf{r}}_i\left(\widetilde{t} + \Delta\widetilde{t}\right) \simeq \widetilde{\mathbf{r}}_i\left(\widetilde{t}\right) + \left(\frac{\mathrm{d}\widetilde{\mathbf{r}}_i}{\mathrm{d}\widetilde{t}}\right)\Delta\widetilde{t} \tag{3}$$

We chose $\Delta\widetilde{t} = 3 \times 10^{-5}$, which corresponds to 20.13 ps with the choice of units shown in Table 1. This also corresponds to the diffusion time over σ_{A}.

Interaction Forces

Four interaction potentials describe excluded volume effects, bond stretch, bending, and torsion.

Table 1 List of major parameters with their symbols and values

Variable	Symbol	Value
Diameter of actin monomers	σ_A	7.0×10^{-9} [m] (1.0)
Viscosity of medium (water, 300 K)	η	0.8599×10^{-3} [kg/m s]
Friction coefficient of actin monomers	ζ_A	5.673×10^{-11} [kg/s] (1.0)
Boltzmann energy (300 K)	k_BT	4.142×10^{-21} [J] (1.0)
Time step	Δt	20.13×10^{-12} [s] (3.0×10^{-5})
Characteristic energy (LJ)	ε	4.142×10^{-21} [J]
Spring constant of F-actin	$\kappa_{s,f}$	0.1691 [N/m] (2,000)
Bending stiffness of F-actin	$\kappa_{b,f}$	1.243×10^{-17} [N m] (3,000)
Torsional stiffness of F-actin	$\kappa_{t,f}$	4.142×10^{-18} [N m] (1,000)
Probability of nucleation	P_n	2.0×10^{-8}, 1.0×10^{-7}, or 1.0×10^{-6}
Nucleation rate constant	$k_{A,n}$	$2.511\times10^{13}\times P_n$ [M^{-1} s^{-1}]
Elongation rate constant	$k_{A,e}$	1.413×10^{9} [M^{-1} s^{-1}]
Depolymerization rate constant	$k_{A,-}$	0.4967 [s^{-1}]
Unbinding rate of ACPs without force	$k^0_{ACP,-}$	0.4967 [s^{-1}]
Damköhler number	Da_n	73.53 ~ 7,371
Initial concentration of actin monomers	C_A	1.51×10^{-4}, 3.59×10^{-4}, 1.21×10^{-3} [M]
Ratio of C_{ACP} to C_A	R	0, 0.125 or 0.5
Number of ACPs bound to two filaments	N_{ACP}	

Stiffnesses of two types of ACPs are given in the text. Numbers in parentheses are the corresponding dimensionless values as defined in the text.

Truncated Lennard-Jones potential A shifted Lennard-Jones (LJ) potential is employed to simulate excluded volume effects between molecules.

$$\widetilde{U}_{LJ}(\widetilde{r}_{12}) = \begin{cases} 4\widetilde{\varepsilon}\left[\left(\frac{\widetilde{\sigma}_{12}}{\widetilde{r}_{12}}\right)^{12} - \left(\frac{\widetilde{\sigma}_{12}}{\widetilde{r}_{12}}\right)^{6}\right] & \widetilde{r}_{12} \le 2^{1/6}\widetilde{\sigma}_{12} \\ 0 & \widetilde{r}_{12} > 2^{1/6}\widetilde{\sigma}_{12} \end{cases} \quad (4)$$

where $\widetilde{\varepsilon}$ is a characteristic energy, $\widetilde{r}_{12}$ is the distance between molecules, $\widetilde{r}_{12} = \|\widetilde{\mathbf{r}}_1 - \widetilde{\mathbf{r}}_2\|$, and $\widetilde{\sigma}_{12}$ corresponds to the average diameter of the two molecules, $\widetilde{\sigma}_{12} = \frac{1}{2}(\widetilde{\sigma}_1 + \widetilde{\sigma}_2)$.

Extensional stiffness of a bond in the chain A bond between two molecules forming a chain is described by a harmonic potential:

$$\widetilde{U}_s = \frac{1}{2}\widetilde{\kappa}_s(\widetilde{r}_{12} - \widetilde{r}_0)^2 \quad (5)$$

where $\widetilde{\kappa}_s$ is a spring constant, and $\widetilde{r}_0$ is the bond length at equilibrium, $\widetilde{r}_0 = \widetilde{\sigma}_{12}$.

In this bead-spring model, higher values of $\widetilde{\kappa}_s$ (thus more stringent control on bond length) would require smaller $\Delta\widetilde{t}$, which would result in higher computational cost. Therefore, for a filament, we use an intermediate value, $\widetilde{\kappa}_{s,f} = 2,000$, producing strains of 0.05 under a force of 60 pN; in experiments, the actual strain under a 60 pN axial force on a filament has been measured to be approximately 0.002 [20, 21]. We confirmed through simulations conducted with higher values of $\widetilde{\kappa}_s$ that the properties analyzed were minimally affected by the lower spring constant.

Bending stiffness Bending rigidity is introduced in terms of a bending potential of the form:

$$\widetilde{U}_b = \frac{1}{2}\widetilde{\kappa}_b(\theta - \theta_0)^2 \quad (6)$$

where $\widetilde{\kappa}_b$ is bending stiffness, θ is the angle formed by three consecutive molecules, and θ_0 is the equilibrium angle. This bending rigidity captures the semi-flexible nature of F-actin in simulation. In addition, once ACPs bind to filaments, bending stiffness is assigned to the ACPs to maintain the desired orientation of binding sites as explained later.

Compared to bond extension, the bending stiffness of filaments, $\widetilde{\kappa}_{b,f}$, is more important for the structural properties of the polymerized network and therefore requires a realistic value. This can be confirmed by measuring the average correlation function of the filament orientation [22]:

$$\langle C(s)\rangle = \langle \cos[\theta(s) - \theta(0)]\rangle = e^{-|s|/L_p} \quad (7)$$

where s is the contour length, and L_p is the persistence length of filaments. Simulating a single 0.9 μm actin filament undergoing thermal motion, L_p was computed to be approximately 20 μm with $\widetilde{\kappa}_{b,f} = 3,000$, close to values measured for F-actin in experiments [22, 23]. In fact, these values satisfy the following relation:

$$L_p = \frac{\kappa_{b,f}\sigma_A}{k_BT} \quad (8)$$

Torsional stiffness Torsional rigidity is introduced to maintain the correct angular position of binding sites along the actin filament:

$$\widetilde{U}_t = \frac{1}{2}\widetilde{\kappa}_t(\phi - \phi_0)^2 \quad (9)$$

where $\widetilde{\kappa}_t$ is torsional stiffness, and Φ is the dihedral angle with an equilibrium (zero torque) value, Φ_0. The method for defining the binding sites is discussed further below.

Torsional stiffness of actin filaments, $\widetilde{\kappa}_{t,f}$, is comparable to bending stiffness [24, 25]. We thus use $\widetilde{\kappa}_{t,f} = 1,000$. This parameter, $\widetilde{\kappa}_t$, also controls the angular orientation between two cross-linked filaments, as described below.

Geometry

Actin monomers Although F-actin forms a double-stranded helix [26], for computational efficiency, we employ a

single-stranded bead-spring model in the simulation [Fig. 1(a)]; a spherical monomer represents two G-actin monomers, and in order to replicate the correct diameter of F-actin, the diameter of the monomer in the model is set to 7 nm. Thus, ten monomers comprise one helical turn reported to be approximately 74 nm [2].

Orientation of the ACP binding site Assuming each G-actin has a single binding site for ACPs, two ACP binding sites are assigned to each monomer on opposing sides. Also, following the helical nature of F-actin, the binding sites rotate around the filament in a right-handed manner, making one full rotation over the length of 10 actin monomers [Fig. 1(b)]. The orientation of these binding sites is maintained by the torsional stiffness of the filament, $\widetilde{\kappa}_{t,f}$, as described by equation (9).

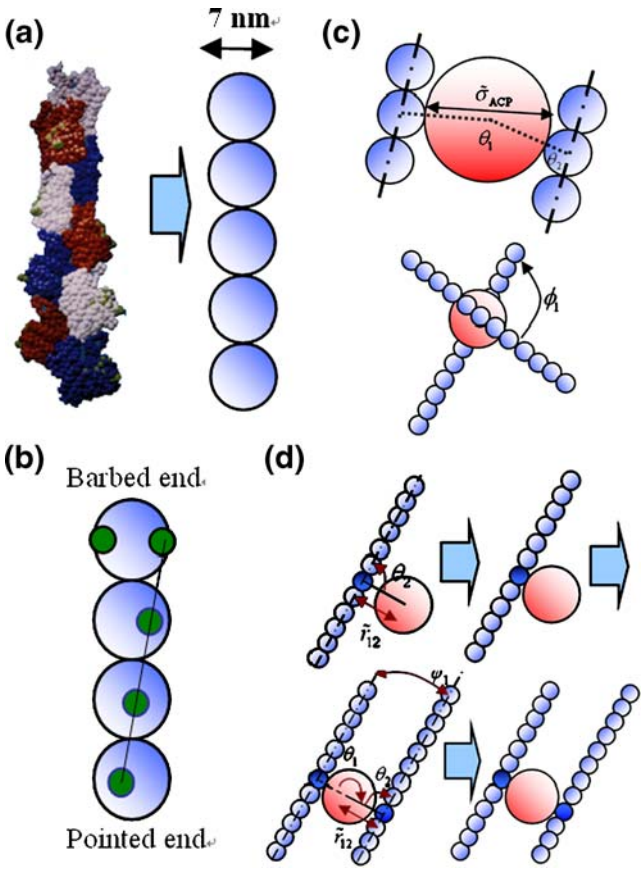

Fig. 1 (**a**) The atomic structure of F-actin (*left*) and the corresponding bead-spring model (*right*). The double-stranded helix is approximated by a single chain of monomers, each corresponding to two G-actins (Reprinted by permission from Macmillan Publishers Ltd: Nature 347: 44–49. © 1990). (**b**) Angular positioning of the ACP binding sites. Binding sites rotate by $\pi/5$ per monomer to account for the helicity of F-actin. (**c**) A cross-link viewed from two orthogonal directions. Four parameters, $\widetilde{\sigma}_{ACP}$, θ_1, θ_2, and Φ_1, determine the geometry of ACPs. (**d**) Cross-link formation. Bonds between one ACP and two monomers are formed only when the distance and angles fall within specified ranges

Actin cross-linking proteins (ACPs) Two types of ACPs are tested: relatively short ACPs that bind filaments in a parallel manner, such as fimbrin, fascin, and α-actinin (termed ACP^B with B denoting "bundle") or long ACPs that form a nearly perpendicular cross-link, such as filamin (termed ACP^C with C denoting "cross"). For simplicity, both types of ACPs are assumed to have a simple, spherical geometry. In Fig. 1(c), σ_{ACP} is the diameter of an ACP, θ_1 is the angle between two bond axes, θ_2 is the angle between a bond axis and the axis of a filament, and Φ_1 is the torsional angle formed by two cross-linked filaments. Additional harmonic potentials are introduced with extensional, bending, or torsional stiffness (denoted by $\widetilde{\kappa}$, with subscripts "s", "b", or "t", respectively) as well as equilibrium values, for ACP^B:

$$\sigma_{ACP} = 1.5, \theta_{1,eq} = \pi, \theta_{2,eq} = \frac{\pi}{2}, \phi_{1,eq} = 0 \qquad (10)$$
$$\widetilde{\kappa}_s = 1,000, \widetilde{\kappa}_{b,1} = 500, \widetilde{\kappa}_{b,2} = 1,000, \widetilde{\kappa}_{t,1} = 500$$

and for ACP^C:

$$\sigma_{ACP} = 3.0, \theta_{1,eq} = 1.158, \theta_{2,eq} = \frac{\pi}{2}, \phi_{1,eq} = \frac{\pi}{2} \qquad (11)$$
$$\widetilde{\kappa}_s = 1,000, \widetilde{\kappa}_{b,1} = 50, \widetilde{\kappa}_{b,2} = 1,000, \widetilde{\kappa}_{t,1} = 50$$

These are chosen by considering structural features of fimbrin and fascin (ACP^B) and filamin (ACP^C), where ACP^C tends to be longer and more flexible.

Polymerization and Cross-linking

Overall simulation setup Periodic boundary conditions are applied to the cubic simulation box. Initially, a specified number of free actin monomers are uniformly placed within the cube, and ACPs are positioned in a random manner. Then, BD simulation as described above is performed, and polymerization is allowed to proceed until only 1% of free actin monomers remain. This criterion is admittedly arbitrary in that the steady state value of free actin monomers would be <1%, given the relative values of the polymerization and depolymerization rate constants. Moreover, at this cut-off time, formation of additional cross-links still occurs slowly due to limited filament mobility. However it was selected so as to minimize computational cost, and properties of the polymerized network are quantified to elucidate effects of various parameters at this point.

Nucleation and growth Nucleation of actin filaments is a slower process than filament growth [3]. This is accounted for by dimerization occurring with a probability, P_n, when two free actin monomers are located within the distance, $\widetilde{r}_{12} = 1.1 \times \widetilde{\sigma}_{12}$. On the other hand, filament elongation

occurs immediately when a free monomer comes within the distance, $\widetilde{r}_{12} = 1.1 \times \widetilde{\sigma}_{12}$, from the barbed end, and the monomer is simultaneously aligned along the filament axis. In reality, the elongation rate depends slightly on filament length (age) and the nucleotide status of free actin monomers [27]. However, to a first approximation, we ignore these effects and assume a constant elongation rate.

It is useful here to clarify how rate constants for nucleation and elongation are computed. An observable rate constant can be influenced by both diffusion and intrinsic reaction mechanisms. For these calculations, nucleation is reaction-limited, whereas elongation is primarily diffusion-limited. From simulation, we obtained empirical expressions for the nucleation rate constant, $k_{A,n}$, and elongation rate constant, $k_{A,e}$.

$$k_{A,n} = 2.51 \times 10^{13} \times P_n\left(M^{-1}s^{-1}\right) \tag{12}$$

$$k_{A,e} = 1.41 \times 10^{9}\left(M^{-1}s^{-1}\right) \tag{13}$$

Depolymerization is also allowed according to a specified unbinding rate constant ($k_{A,-}$) but rarely occurs on the time scale of this simulation.

Cross-linking Cross-linking of two filaments by an ACP occurs via the following two steps. First, an ACP binds to a monomer of a filament under the following conditions:

$$\begin{aligned} &\widetilde{r}_{A-ACP} \le 1.1 \times \frac{(\widetilde{\sigma}_A + \widetilde{\sigma}_{ACP})}{2}, \\ &\left|\theta_1 - \theta_{1,eq}\right| \le 0.1745(10^\circ), \\ &\left|\theta_2 - \theta_{2,eq}\right| \le 0.1745 \end{aligned} \tag{14}$$

where $\widetilde{r}_{A-ACP}$ is the distance between an actin monomer and an ACP.

Next, a cross-link is formed when the filament-bound ACP binds to a monomer that is a part of another filament under the conditions in equation (14), plus:

$$\left|\phi_1 - \phi_{1,eq}\right| \le 0.1745 \tag{15}$$

In this model, unbinding of ACPs occurs according to Bell's equation [28]:

$$k_{ACP,-} = k^0_{ACP,-} \exp\left(\frac{\gamma F_b}{k_B T}\right) \tag{16}$$

where $k^0_{ACP,-}$ is a zero-force unbinding rate constant, γ is the mechanical compliance of the bond between ACP and a monomer of the filament, and F_b is the applied force on the ACP-monomer bond.

Characterization of Polymerized Structures

Polymerization time Polymerization time, t_p, is defined as the time required to incorporate 99% of actin monomers into filaments. As shown below, t_p is a function of $k_{A,n}$, provided the Damköhler number [29]:

$$Da_n \equiv \frac{t_n}{t_d} = \frac{1/k_{A,n}C_A}{\zeta_A r_0^2/6k_B T} \gg 1 \tag{17}$$

where t_n is the nucleation time, and t_d is the diffusion time over r_0, the initial separation distance between actin monomers, where $r_0 = (500 \times N_{AVO} \times C_A)^{-1/3}$ (N_{AVO} is Avogadro's number).

A dimensionless polymerization time is then:

$$\widetilde{t}_p \equiv \frac{t_p}{\zeta_A \sigma_A^2/k_B T} = \frac{t_p[s]}{6.711 \times 10^{-7}} \tag{18}$$

Filament length From equilibrated networks, the distribution of filament length, L_f, is analyzed and expressed in normalized form, L_f/σ_A.

Distances between active ACPs L_c is defined as the distance between two ACPs which cross-link two filaments, and its corresponding dimensionless form is $\widetilde{L}_c = L_c/\sigma_A$. In structures containing ACP^C, L_c can be considered an alternative measure of pore size with its variance as a measure of network inhomogeneity. In the case of bundled networks, L_c is largely determined by the prescribed spacing between cross-links on bundled filaments. Consequently, the difference in the distribution of L_c is a useful means to distinguish the two types of networks.

Cross-linking angle Angular distributions between two cross-linked filaments, Φ_1, are measured at the point of cross-linking, which ranges between 0 and π.

Network connectivity Connectivity of the actin cytoskeleton is considered an important property for mechanotransduction and signal transmission [30] and is evaluated using the adjacent matrix technique. Each filament is numbered from 1 to N, where N is the total number of filaments. Then, an $N \times N$ matrix, $\mathbf{Q}$, is created such that all elements along its diagonal and below are zero. The value of an element above the diagonal, $\mathbf{Q}_{i,j}$, is either one or zero depending on whether the ith and jth filaments are cross-linked (1) or not (0). This matrix has the property that, if the matrix is multiplied by itself k times, the sum of all elements in the resultant matrix, $\sum_{i,j} \mathbf{Q}^k|_{i,j}$, indicates how many sets of $k+1$ filaments are connected by ACPs. Therefore, the sum provides information about the degree of connectivity corresponding to percolation, which in turn relates to the mechanical stiffness of a random elastic network [31–33].

Pore size A particularly useful parameter in the context of transport through the network is pore size distribution. This is measured by placing many small spheres uniformly

within the network, increasing their diameters until contacting the surrounding filaments, and finally, adjusting their center position so that maximum possible growth is achieved within each pore. Redundant spheres are eliminated, and the diameters of remaining spheres are regarded as those of pores. Pore size can be expressed in a dimensionless form, L_{pore}/σ_A.

Properties of bundles Actin bundling and the formation of stress fibers are common in response to mechanical stimuli, often occurring near the leading edge in a migrating cell, and they have important implications to cell stiffness. Consequently, the process of bundling by ACP^B is of particular interest. Here, we evaluate the length and effective diameter of bundles; bundle length is taken as the maximum end-to-end distance of the entire collection of filaments in a given bundle. The effective diameter of a bundle ignoring the size of the ACPs is $\sigma_b = \sqrt{N_{f,b}}\sigma_A$, where $N_{f,b}$ is the effective number of filaments in the cross-section of a bundle, defined as sum of all filament lengths in the bundle divided by its end-to-end contour length.

Results

Overall Network Morphology

Two examples of polymerized structures cross-linked by ACP^B and ACP^C are provided in Fig. 2, showing only those filaments in cross-linked structures with connectivity ≥3. Several characteristic differences can readily be seen. Since ACP^C link more filaments, the network in Fig. 2(b) looks much denser. Bundles are clearly visible when ACP^B are used, but the extent of bundling is somewhat less than might be expected based on observations of thick stress fibers *in vivo* (see discussions). ACP^C generate more homogeneous networks, although this needs to be reassessed when all filaments are present, using measures such as pore size distributions.

Dependence on System Size

While the use of periodic boundary conditions should minimize the adverse consequences of a small computational domain, certain effects, such as bundling into larger fibers, may not be accurately captured if the domain is too small. In addition, a small domain can lead to larger statistical variations in the properties we analyze to characterize the network. We used variability in filament length, L_f, to measure simulation consistency and to determine the trade-off between the accuracy of a large system and the numerical uncertainty of a smaller one. As seen in Fig. 3, increasing the system size results in more consistent results; $<L_f/\sigma_A>$ approaches a well-defined value and exhibits less fluctuation. This corresponds to an increase in the number of actin monomers from 512 to 27,000. Based on this, we chose to conduct all simulations using a computational domain containing 8,000 actin monomers. The corresponding domain size depends on C_A used in each condition, ranging from $40\sigma_A$ (C_A=1.21 mM) to $80\sigma_A$ (C_A=151 μM).

Analysis of Polymerized Structures

There are many independent parameters in the model. However, we chose and systematically combined the following values to examine their effects on resulting structures:

1. Nucleation rate constant: Da_n=73.53~7,371 (P_n=1×10^{-6}, 1×10^{-7}, or 2×10^{-8})
2. Initial concentration of actin monomers: C_A=151 μM, 359 μM, or 1.21 mM

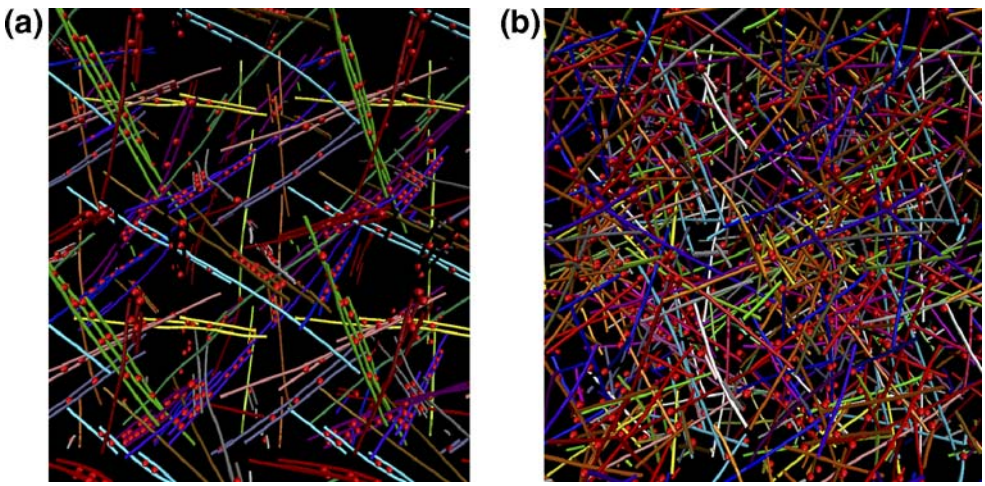

Fig. 2 Examples of polymerized structures: (**a**) ACP^B and (**b**) ACP^C at C_A=151 μM, Da_n=7,371 and R=0.5; ACPs (*red spheres*) and filaments (*rods*). To emphasize the cross-linked structures, only sets of filaments cross-linked by ACPs (connectivity≥3) are displayed with different colors indicating separate sets of cross-linked filaments. Simulation boxes are duplicated in each direction to better visualize the bundles, so the width of the figure is 1.12 μm (560 nm×2). For visualization, VMD is used [47]

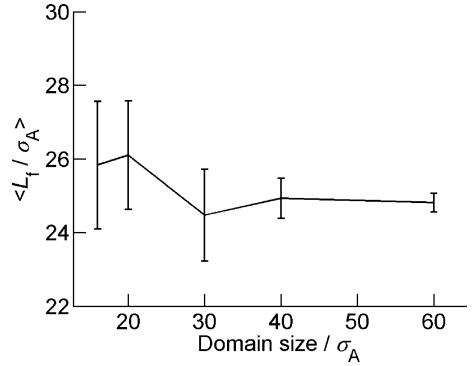

Fig. 3 Dependence of the mean filament length on the system size at Da_n=73.53 and C_A=1.21 mM, where the domain size means the width of cubical computational domain

3. Ratio of ACP-to-actin concentration: $R=C_{ACP}/C_A=0$, 0.125, or 0.5
4. Type of ACP: pure ACP^B, pure ACP^C, or half ACP^B and half ACP^C

From the above parameter values, we selected 51 independent simulations. For plotting results in dimensionless format, we introduce the volume or solid fraction, Φ, as a dimensionless initial concentration of actin monomer:

$$\Phi = 54.06 \times C_A[\mathrm{M}] \tag{19}$$

Polymerization time In all conditions tested, $\tilde{t}_p$ is much shorter than the values observed in experiments. This difference is due to larger $k_{A,n}$ and $k_{A,e}$ used in the simulation for computational efficiency. However, if the ratio between $k_{A,n}$ and $k_{A,e}$ is chosen properly, the resultant polymerized structure in the simulation should be similar to the real one. Differences might still exist, though, due to "aging" of the network associated with adjustments over time that would naturally occur as cross-links break and reform.

$\tilde{t}_p$ depends on Da_n and Φ as in Fig. 4(a), and plotting $\tilde{t}_p\Phi^{5/6}$ versus Da_n causes the curves to collapse [Fig. 4(b)], which suggests the scaling:

$$\tilde{t}_p \sim \Phi^{-5/6} Da_n^{1/2} \sim C_A^{-5/6}\left(k_{A,n}^{-1} C_A^{-1/3}\right)^{1/2} \sim \frac{1}{k_{A,n}^{1/2} C_A} \tag{20}$$

Filament length Computed distributions of L_f are shown in Fig. 5(a), the mean values of which [Fig. 5(b)] can be collapsed into a single master curve [Fig. 5(c)] using the following scaling relation:

$$\langle L_f/\sigma_A \rangle \sim \left(Da_n \Phi^{1/3}\right)^{1/2} \sim \frac{1}{k_{A,n}^{1/2}} \tag{21}$$

This shows that both $\langle L_f/\sigma_A \rangle$ and $\tilde{t}_p$ scale as $k_{A,n}{}^{-1/2}$.

Distances between active ACPs The distributions of L_c for different ACP types highlight differences in the resulting networks. Results show that the distribution for networks containing ACP^B has two peaks at about $5\sigma_A$ and $10\sigma_A$ [Fig. 6(a)] corresponding to the distance between bundling cross-linkers located between two filaments every half or full helical turn [cf. Fig. 1(b)]. This is consistent with electron microscopy [2, 34]. By comparison, the distribution of L_c for ACP^C is significantly different, decreasing monotonically without any distinguishable peaks, and generally having a wider distribution, although this is somewhat dependent on the particular parameter values used [Fig. 6(b)].

For larger Da_n, filaments are longer, leading to an increase in the range of L_c as large L_c can occur only with long filaments. Also, the number of ACPs that actually cross-link filaments (active ACPs), N_{ACP}, can influence the overall count in the y-axis of Fig. 6.

Cross-linking angle Cross-linking angle is an indicator of whether the network consists of filaments that are largely bundled or are arranged in a more random, homogeneous fashion, and it is primarily determined by the type of ACP.

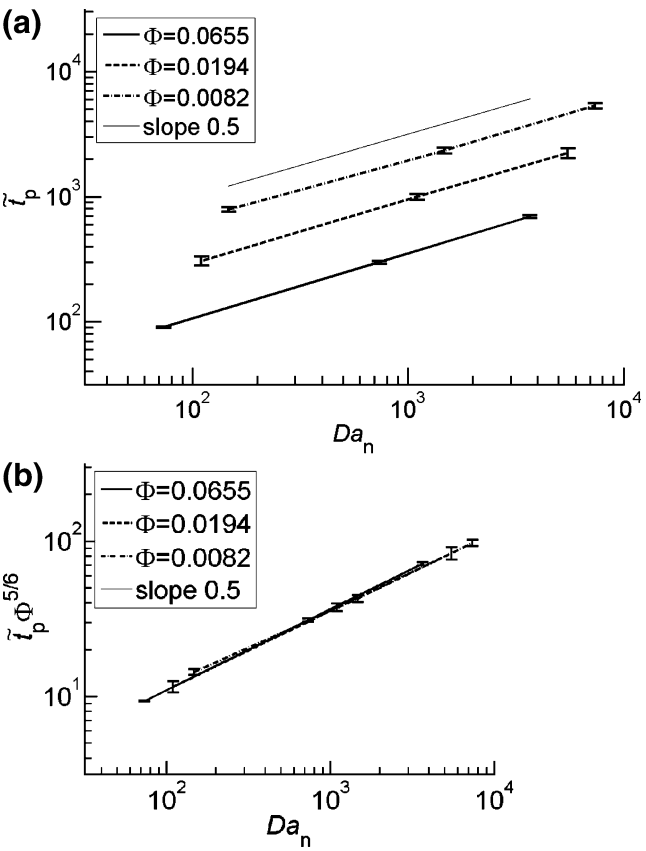

Fig. 4 (**a**) $\tilde{t}_p$ as a function of Da_n. Unless noted otherwise, error bars in all subsequent figures (Figs. 5 and 8) are obtained from the 51 combinations of the four parameters mentioned in text. The top line has a slope of 0.5. (**b**) Same data as in (**a**), but with $\tilde{t}_p$ multiplied by $\Phi^{5/6}$

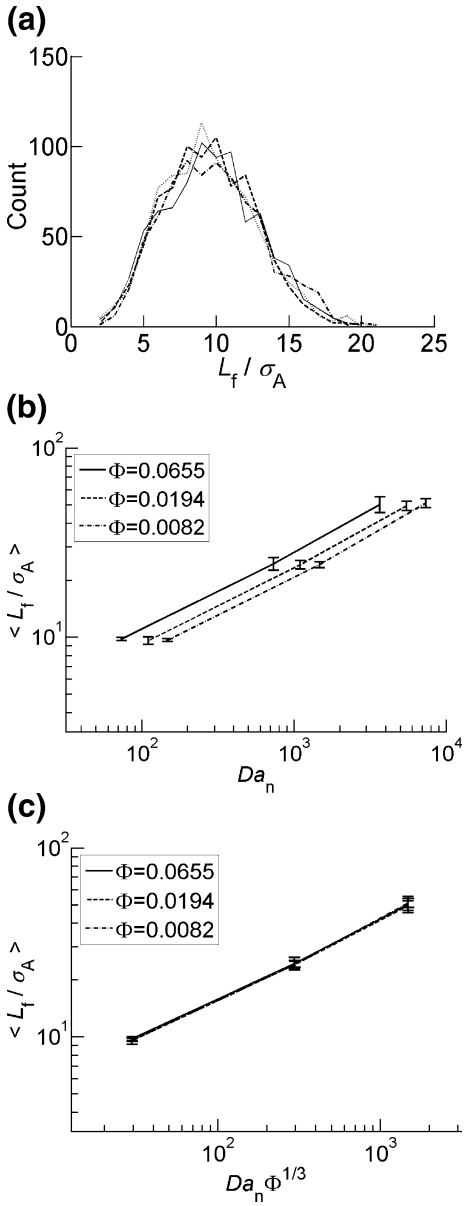

Fig. 5 (**a**) Sample filament length distributions for four different simulations at Da_n=147.4 and C_A=151 μM. (**b**) Mean filament length as a function of Da_n for three different solid fractions. (**c**) Same data as in (**b**), but with Da_n multiplied by $\Phi^{1/3}$ to illustrate the scaling with concentration

For ACP^B, the average cross-linking angle is −2.39±3.98° (close to 0), and the standard deviation is relatively narrow due to large $\widetilde{\kappa}_{t,1}$. By comparison, for ACP^C, the average is 87.5±10.5° (close to $\pi/2$), where the larger standard deviation is due to the smaller value of $\widetilde{\kappa}_{t,1}$.

Connectivity Connectivity is a measure of the extent to which the network is cross-linked, and its degree is evaluated by using the adjacent matrix method explained above. For example, in the projected image of Fig. 7(a), one collection of seven cross-linked filaments (connectivity=7) is highlighted. In this particular case, the cross-linked structure extends nearly all the way across the computational domain (outer box). This example is taken from a simulation using ACP^C, so all filaments are seen to form nearly right angles at cross-link points.

The degree of connectivity, measured by the sum of all elements in the resultant matrix $\left(\sum_{ij} Q^k|_{i,j}\right)$, varies widely with the number of functional cross-links, so data are first normalized by dividing the number of clusters with a given connectivity by the number of clusters with connectivity=2. It is apparent that the degree of connectivity for networks with ACP^C is greater than that with ACP^B [Fig. 7(b) and (c)]. In addition, connectivity of networks cross-linked by ACP^C depends on Da_n [Fig. 7(b)], whereas Da_n has little effect on the network with ACP^B. This is because longer filaments have a greater opportunity to form extended structures with high connectivity when cross-linked at right angles than shorter filaments.

Pore size Mean pore size, $<L_{pore}>$, is proportional to $C_A^{-1/3}$ [Fig. 8(a)]; *i.e.*, proportional to r_0, and the relationship is relatively unaffected by the type of ACPs used in the simulation, at least for the range of conditions tested here.

However, differences can be seen in the shapes of the distribution with ACP^B tending to have a broader spread with a lower peak. This suggests, as one would expect, that

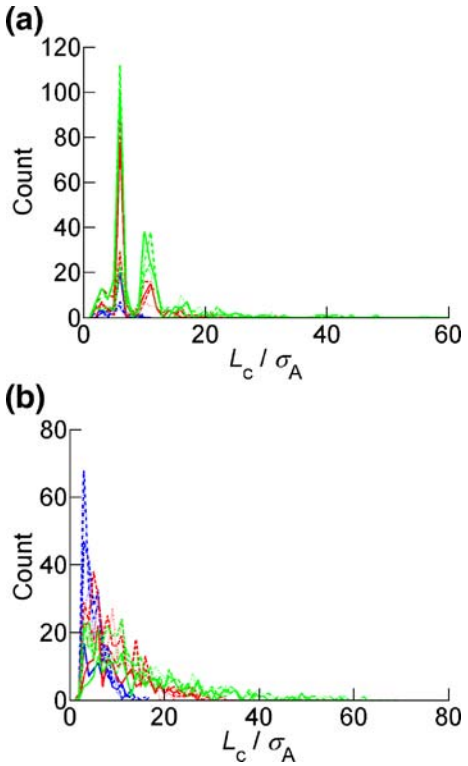

Fig. 6 (**a**) Distribution of distances between active ACPs of 12 bundled structures (ACP^B). Each of the 12 structures has a condition that is a set of three parameters: Da_n=73.53~7,371 (P_n=1×10^{-6}, 1×10^{-7}, or 2×10^{-8}), C_A=151 μM or 359 μM, R=0.125 or 0.5. (**b**) 12 structures cross-linked by ACP^C. Conditions for the structures are the same as part (**a**) except that ACP^C is used

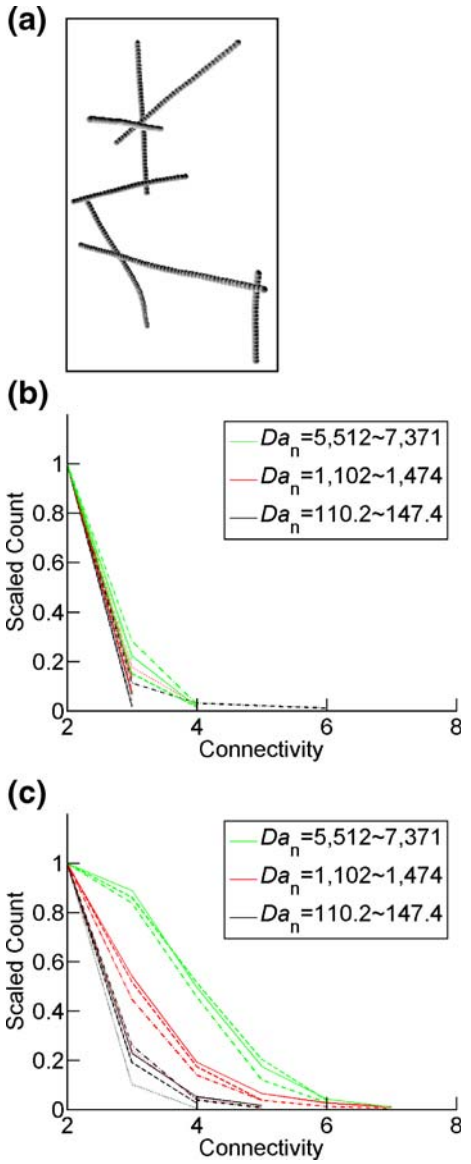

Fig. 7 (**a**) An example of percolation at Da_n=7,371, C_A=151 μM, and R=0.5. The outer box corresponds to the computational domain whose width is 560 nm. Among all filaments in the box, only seven filaments cross-linked by ACP^C are shown, and they mostly cross the domain from one boundary to the other. (**b**) Distribution of the network connectivity, with ACP^B at R=0.125 or 0.5, C_A=151 μM or 359 μM, scaled by the number of filaments with connectivity 2. Each color represents a different P_n and thus a different Da_n (Da_n slightly depends on C_A with the same P_n). (**c**) The same distribution for ACP^C, showing stronger dependence on Da_n

ACP^C tend to produce networks with a more homogeneous distribution of pore sizes, while the broader distribution with ACP^B arises from the fact that pores can exist either near the branchings of bundled filaments or between bundles. This tendency is most accentuated when filaments are long (large Da_n) compared to the size of the simulation box.

Length and diameter of bundles Bundle length is primarily a function of Da_n at the time when the simulations are terminated, and it tends to be somewhat less than twice the average filament length (1.5 for small Da_n, 1.7 for medium Da_n, 1.9 for large Da_n). This is consistent with the observations that the mean effective diameter of bundles falls within a narrow range ($1.5\sigma_A$~$2.3\sigma_A$; slightly larger value with smaller C_A), and that connectivity falls off abruptly for values greater than two. As discussed further below, this result might have been influenced by the fact that N_{ACP} was still increasing when the simulations were stopped.

Effects of Other Parameters on the Network Structure

Two additional parameters were varied, but less systematically than in the cases above. Here, we summarize their effects using a baseline case for which all the other parameter values are held constant.

Bending stiffness Filament bending stiffness, $\tilde{\kappa}_{b,f}$, was selected to produce a persistence length comparable to the actual value. We tested its effect by reducing it tenfold $\left(\tilde{\kappa}_{b,f} = 3,000 \rightarrow 300\right)$ in the following conditions.

Da_n=1,474, C_A=151 μM (constant), R=0.125 or 0.5
ACP type=pure ACP^B, pure ACP^C, or a mixture with half of each.

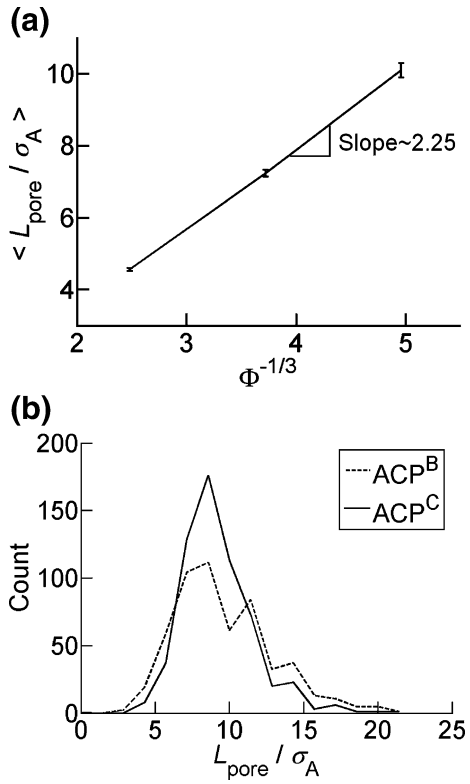

Fig. 8 (**a**) Mean pore size versus $\Phi^{-1/3}$. (**b**) Pore size distribution at Da_n=7,371, C_A=151 μM, and R=0.5

Noticeable differences were changes in $<L_f/\sigma_A>$ by +10%, $\tilde{t}_p$ by −8%, N_{ACP} by +38%, and an increase in connectivity (Fig. 9).

These changes are due to the fact that when the filaments are allowed to fluctuate more, their barbed ends undergo greater diffusive motions and thus encounter more free monomers for elongation. Subsequently, quicker elongation causes a reduction in polymerization time and greater filament length. Furthermore, flexible filaments can more easily satisfy geometric conditions for cross-linking, resulting in an increase in N_{ACP} and a consequent increase in connectivity.

Size of ACP^C In our simulation, ACP^C is three times as large as that of actin monomers, reflecting their actual relative sizes. It is possible, however, that the large diameter could influence the nature of the polymerized structures. Therefore, we reduced its diameter from $3\sigma_A$ to σ_A and ran simulations in the following four conditions:

Da_n=1,102 (359 μM) or 1,474 (151 μM) ($P_n=1.0\times10^{-7}$)
C_A=151 μM or 359 μM, R=0.125 or 0.5

ACP type=pure ACP^C

This resulted in changes in $<L_f/\sigma_A>$ by +8%, $\tilde{t}_p$ by −9%, and variations in N_{ACP} and connectivity [Fig. 10(a) and (b)]

At high C_A and high Da_n, $<L_f/\sigma_A>$ is affected since filament elongation is hampered by other filaments and ACPs. Likewise, the assumed size of ACP^C is large compared to an actin monomer, so the free ACPs may lead to volume exclusion effects, which can limit monomer access to the barbed ends of filaments and thereby reduce the effective rate of elongation. Thus, $\tilde{t}_p$ may be reduced with smaller ACPs.

The variation in N_{ACP} is more complicated. We expected that N_{ACP} would decrease at all four conditions due to the narrower binding region for filaments. However, while at R=0.125, N_{ACP} is decreased, at R=0.5, it is increased. One possible explanation is that the increase at R=0.5 is caused by the reduced volume exclusion effects. In other words, the system is too crowded for ACP^C to easily bind filaments when larger ACPs are used. Therefore, reduction in volume exclusion appears to be more important than the reduction in the filament binding sites in ACP^C. Connectivity naturally decreases at R=0.125 but is enhanced at R=0.5 due to the changes in N_{ACP}.

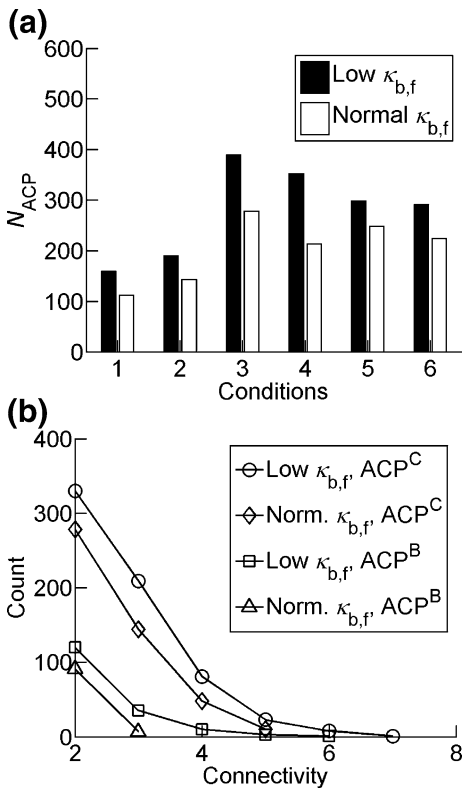

Fig. 9 Variations in (**a**) N_{ACP} and (**b**) connectivity as a function of bending stiffness. Conditions on the x-axis in (**a**) are: (Da_n=1,474 and C_A=151 μM for all cases; 1, 3, 5: R=0.125 and 2, 4, 6: R=0.5; 1, 2: ACP^B, 3, 4: ACP^C, and 5, 6: half ACP^B and half ACP^C)

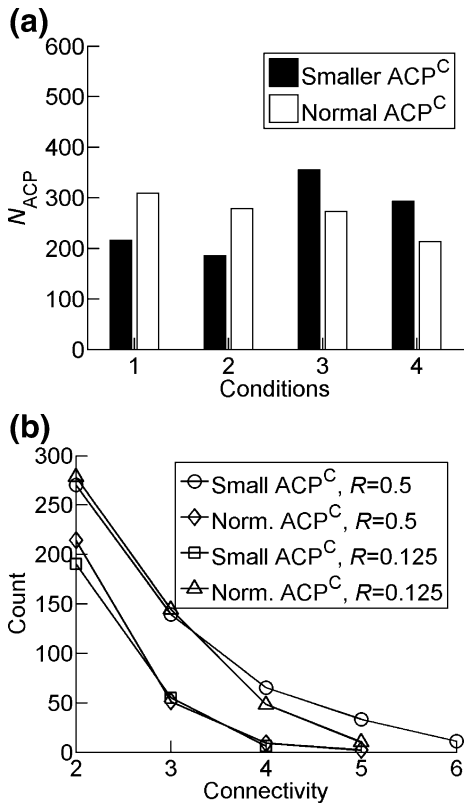

Fig. 10 Variations in (**a**) N_{ACP} and (**b**) connectivity as a function of the size of ACP^C. Conditions on the x-axis in (**a**) are: (Da_n=1,102~1,474 ($P_n=10^{-7}$) for all cases; 1, 3: C_A=359 μM and 2, 4: C_A=151 μM; 1, 2: R=0.125 and 3, 4: R=0.5)

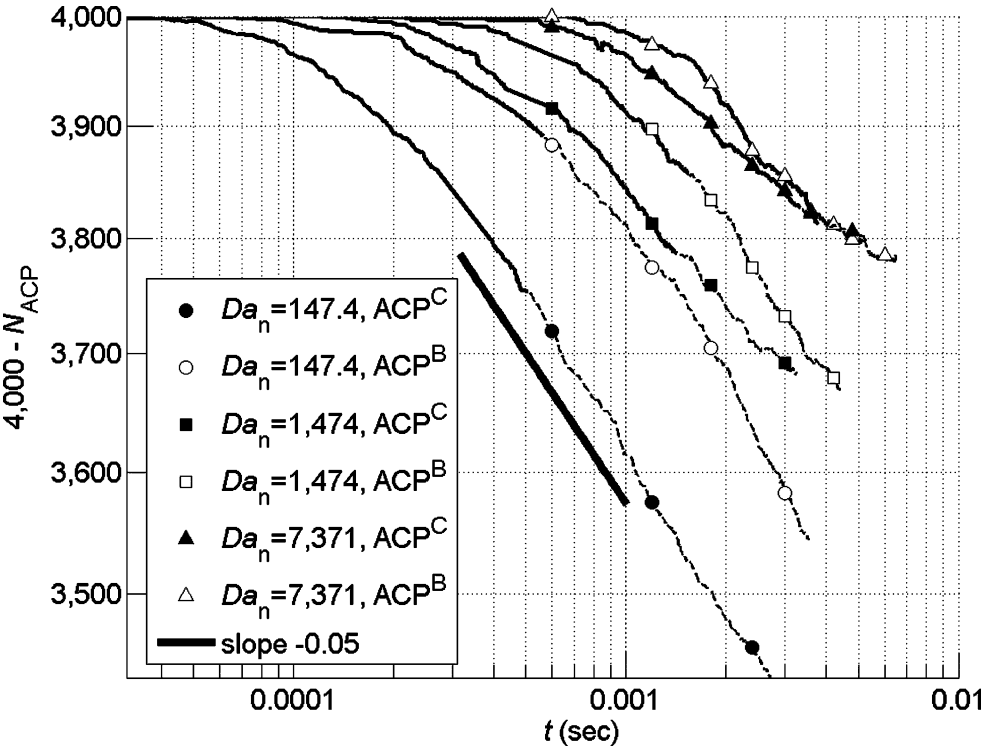

Fig. 11 Number of ACPs not bound to two filaments for six cases with C_A=151 μM and R=0.5 (4,000 ACPs). Bold lines show polymerization up to the end point when the simulations stopped, and dash lines correspond to longer simulations after it. All curves exhibit the power–law behavior of −0.05 at intermediate time range. The two curves with the highest Da_n appear to approach a steady state

Polymerization Dynamics

Although simulations were continued until 99% of monomers were incorporated into filaments, there is no guarantee that the network has achieved a steady state. Another measure that we examined was the number of ACPs that were either free in solution or bound to a single filament and therefore still available to cross-link two filaments. Using this measure, the network is clearly still evolving at the time the simulations were terminated, although the rate of continued evolution was a weak function of time, varying as $t^{-0.05}$ (Fig. 11). Due to the small range of variation in "4000-N_{ACP}", it is difficult to distinguish power-law from exponential behavior in these results.

Discussion

Significance of Models

It is widely recognized that polymerized actin can take on a variety of conformations within the cell, controlled by a mix of actin cross-linking, branching, capping, and severing proteins, among other factors. They range from nearly isotropic networks to highly aligned filament bundles such as stress fibers. While various structures have been observed, little is understood regarding their assembly. Here, we use a minimalistic approach by using only actin monomers and two types of ACPs, and by simplifying the actin filament structure, all with the intent of examining the factors that might influence network morphometry. While these simplifications preclude a truly realistic representation of the actin cytoskeleton, the results should still prove useful for understanding how the network structure is regulated. Moreover, the present model can be extended for simulating other essential processes after modifications, such as force transmission through cells and mechanotransduction.

Parameters of ACPs

We employed two kinds of ACPs having different parameter values to represent two major groups of ACPs: ACP^B, bundling filaments in parallel and ACP^C, cross-linking filaments at nearly a right angle. Each ACP produced a characteristic network and yielded different distributions of properties, such as cross-linking angle L_c, and connectivity. However, the effects of the other parameters related to ACPs $\left(\sigma_{ACP}, \theta_{2,eq}, \widetilde{\kappa}_s, \widetilde{\kappa}_{b,1}, \widetilde{\kappa}_{b,2}, \widetilde{\kappa}_{t,1}\right)$ were not systematically investigated in the present study although they are known to affect various network properties [35–37]. In addition, while the atomic structures of many ACPs are currently known, many questions remain regarding the mechanism of cross-linking and what factors govern network morphology. For instance, why filamin tends to form an orthogonal network at low concentrations but produces bundles when filamin concentration is increased [38], is not yet clearly understood. Further studies will be needed to elucidate these important issues.

Filament Bundling

One of the major questions that this model can address is the transition from a homogeneous network to a bundled network containing stress fibers, each comprised of a large number of small filaments. In the present simulations, bundles typically contained no more than a few individual filaments. This is partly because the simulations were terminated before reaching a true steady state; while actin polymerization is completed on a relatively short time scale, binding of ACPs and subsequent cross-linking of filaments occur more slowly, and the network was continuing to evolve at the end of the simulation (Fig. 11). In those few simulations that were carried out for a longer time, we observed some further bundling, but the excessive computational requirements of these longer simulations precluded a comprehensive study. The small system size (280 ~ 560 nm) also made it difficult to simulate the formation of stress fibers in cells, whose diameter can be as large as 500 nm.

When the network is subjected to mechanical strains, two new effects will arise. First, bonds will rupture more readily, following Bell's equation. Second, once a bond ruptures, the network will locally reorganize, resulting in alignment of filaments in the direction of stress [39]. This provides a natural mechanism for stress fiber formation and will also contribute to network annealing.

Annealing of Networks

As discussed above, our criterion for terminating the simulation was based on the number of monomers left after polymerization, which was not a steady state with regard to cross-linking events within the network. While this has little effect on either mean polymerization time or mean filament length [equations (20) and (21)], other quantities related to the extent of cross-linking, such as N_{ACP}, L_{c}, and connectivity could be affected by the choice made for the end point of the simulation. Furthermore, there is an additional issue of the strong dependence of the total simulation time on Da_{n}. To investigate such possible effects, we carried out a few simulations with different conditions for longer times.

While Fig. 11 demonstrates that the number of active cross-links continues to slowly evolve, the behavior depicted in the figure provides an approximate means for estimating the time to full equilibration. In this context, equilibration can be viewed as the state in which the formation of new cross-links is balanced by their unbinding rate. If the network were athermal, then the unbinding rate would simply be characterized by the rate constant, $k^0_{ACP,-}$. Due to thermal fluctuations, combined with the use of Bell's equation, the actual rate of unbinding is found in the simulation to be considerably higher, with effective rate constants as determined from the simulations: approximately 100 and 30 s^{-1} for ACP^B and ACP^C, respectively. An estimate of the time for equilibration can then be obtained by equating the unbinding rate as determined from these estimates to the bond formation rate as characterized by the power-law behavior in Fig. 11. This leads to values of about 5 and 10 ms for ACP^B and ACP^C, respectively. One simulation with ACP^B and the highest Da_{n} in Fig. 11 almost reaches this estimate, and N_{ACP} seems to approach a plateau. While this does not necessarily imply that network annealing could not cause further evolution in the network, it does demonstrate the existence of a longer characteristic time than would have been inferred from the rate constants alone.

Implications for Cytoskeletal Rheology

The power-law dependence apparent in Fig. 11 is of particular interest, and is potentially relevant to two as yet unexplained tendencies observed in cytoskeletal networks. One observation is that cells exhibit a phenomenon termed fluidization under high degrees of shear, characterized by a sudden drop in shear modulus that recovers on a time scale of minutes. This has been observed in fibroblasts [40], neutrophils [41], and human airway smooth muscle cells tethered to a flexible substrate and suddenly subjected to strain [42]. Under the high strains used in these experiments, cross-links are likely broken, and they would then recover (reform) on a time scale determined by the formation of new cross-links, characterized by the long time power-law behavior associated with network reorganization rather than the much shorter time scales determined by $k_{\mathrm{ACP,on}}$ for ACPs free in solution. This phenomenon has also been termed "healing" in the sense that the ruptured matrix heals by the gradual (re-)formation of broken cross-links. A second observation is that cells exhibit power-law rheology with no apparent intrinsic timescale. Due to active actomyosin contractions present in all living cells, cross-links will be ruptured, and subsequently reform at a rate in excess of the normal unbinding rate, following a behavior such as that of Bell's law [equation (16)]. Creation of new bonds would not behave as a first order reaction, but would instead follow the power-law behavior of Fig. 11. While the direct link between these two phenomena is not yet clear, it is intriguing to speculate about a possible connection.

Potential Refinements of the Model

Nucleation Since one monomer represents two G-actins, a dimer has been assumed to constitute a stable nucleus in the simulation, whereas it has been demonstrated that a trimer of

G-actins forms a critical nucleus [3, 4]. We find that $<L_f/\sigma_A>$ is independent of C_A because both average nucleation and elongation rates are linearly proportional to C_A. However, this might not be true in experiments. In contrast to the dimer nucleus model, a trimer nucleus model will have two lag phases, causing the nucleation rate to depend more strongly on C_A, as has been demonstrated by experiments and simulations [3]. In the event that the two average rates depend differently on C_A, $<L_f/\sigma_A>$ will likely vary with C_A. The current model could capture more realistic behavior by employing two lag phases or letting the nucleation probability depend on C_A.

Friction coefficient In the present simulation, the friction coefficient of actin monomers, ζ_A, is assumed to be $\zeta_A = 3\pi\eta\sigma_A$, according to the simple Stokes-Einstein relation, regardless of whether they are free in solution or have been incorporated into a filament. In reality, the friction coefficient differs if the monomers become a part of a filament due to hydrodynamic interactions, and it also depends on the filament length. Also, hydrodynamic interactions between filaments can alter frictional drag [43]. In addition, unlike a spherical object, the friction coefficient of the filament depends on the direction of external flow. These effects can all be incorporated, but they increase the complexity of the model with a consequent reduction in computational efficiency.

Electrostatic interaction Strictly speaking, because actin monomers and filaments have nonzero charge, electrostatic interactions will be present and should be accounted for in the simulation. These effects can alter actin dynamics as a result of variations in salt concentration [44, 45]. Again, such effects could be included, but not without incurring enormous computational costs associated with these long-range interactions.

Validation of parameters In the present simulation, values of parameters are taken from independent measurements wherever possible, or validated by comparison to other experiments. In some cases, however, no such empirical support could be found, so the values are not rigorously verified. Further single molecule measurements and molecular dynamics simulation will aid in more accurate estimation of these parameters, which are currently being actively pursued.

Computational domain size and attainable time range Current simulations are restricted to small domains (~560 nm) and short times (1~10 ms). Although we considered the finite size effect, further investigation is necessary. In addition, as mentioned above, large bundles or annealing of networks were not observed. To resolve these limitations, parallel processing schemes would be necessary. In addition, further coarse-graining, as might be accomplished by transforming segments of the actin filament into cylindrical segments, is currently being developed. The combined benefits of parallel processing and further coarse-graining promise considerable enhancement in efficiency.

Applications and Future Work

Our model has the potential to be used to simulate a variety of other actin-related phenomena, e.g., to gain insight into the variations of viscoelastic modulus in actin gels [46], which is typically quantified in terms of the complex shear modulus over a range of frequencies from $0.1 \sim 10^4$ Hz. To this end, we are currently analyzing thermal motions of the filaments. Furthermore, new insights into cell motility and lamellipodium protrusion are possible. As a long-term goal, the simulation of mechanotransduction through focal adhesions and cell–cell junctions can be performed by adding membranes and transmembrane proteins, such as integrin and talin. These have the potential as a multi-scale model for elucidating the mechanism of force transduction *in vivo*.

Acknowledgments We gratefully acknowledge support of the NIH (GM076689) and a fellowship to TYK from the Samsung Scholarship Foundation.

References

1. Howard J (2001) Mechanics of motor proteins and the cytoskeleton. Sinauer Associates, Sunderland, MA.
2. Lodish H, et al (2003) Molecular cell biology, 5th edn. W. H. Freeman and Company, New York, NY.
3. Sept D, McCammon JA (2001) Thermodynamics and kinetics of actin filament nucleation. Biophys J 81(2):667–674.
4. Cooper JA, et al (1983) Kinetic evidence for a monomer activation step in actin polymerization. Biochemistry 22(9):2193–2202.
5. Mofrad MRK, Kamm RD (2006) Cytoskeletal mechanics: Models and measurements. Cambridge University Press, New York, NY.
6. Kreis T, Vale R (1999) Guidebook to the cytoskeletal and motor proteins, 2nd edn. Oxford University Press, New York, NY.
7. Le Y, Sept D, Carlsson AE (2006) Energetics and dynamics of constrained actin filament bundling. Biophys J 90(12):4295–4304.
8. Chu JW, Voth GA (2005) Allostery of actin filaments: Molecular dynamics simulations and coarse-grained analysis. P Natl Acad Sci USA 102(37):13111–13116.
9. Chu JW, Voth GA (2006) Coarse-grained modeling of the actin filament derived from atomistic-scale simulations. Biophys J 90 (5):1572–1582.
10. Sept D, Elcock AH, McCammon JA (1999) Computer simulations of actin polymerization can explain the barbed-pointed end asymmetry. J Mol Biol 294(5):1181–1189.
11. Carlsson AE (2006) Stimulation of actin polymerization by filament severing. Biophys J 90(2):413–422.
12. Yu XP, Carlsson AE (2003) Multiscale study of counterion-induced attraction and bundle formation of F-actin using an ising-like mean-field model. Biophys J 85(6):3532–3543.

13. Yu XP, Carlsson AE (2004) Kinetics of filament bundling with attractive interactions. Biophys J 87(6):3679–3689.
14. Atilgan E, Wirtz D, Sun SX (2006) Mechanics and dynamics of actin-driven thin membrane protrusions. Biophys J 90(1):65–76.
15. Gov NS, Gopinathan A (2006) Dynamics of membranes driven by actin polymerization. Biophys J 90(2):454–469.
16. Shlomovitz R, Gov NS (2007) Membrane waves driven by actin and myosin. Phys Rev Lett 98(16):168103-1–168103-4.
17. Reif F (1965) Fundamentals of statistical and thermal physics. McGraw-Hill, New York, NY.
18. Underhill PT, Doyle PS (2004) On the coarse-graining of polymers into bead-spring chains. J Non-Newton Fluid Mech 122(1–3):3–31.
19. Liao Q, Dobrynin AV, Rubinstein M (2003) Molecular dynamics simulations of polyelectrolyte solutions: Nonuniform stretching of chains and scaling behavior. Macromolecules 36(9):3386–3398.
20. Kojima H, Ishijima A, Yanagida T (1994) Direct measurement of stiffness of single actin-filaments with and without tropomyosin by in-vitro nanomanipulation. P Natl Acad Sci USA 91(26):12962–12966.
21. Higuchi H, Yanagida T, Goldman YE (1995) Compliance of thin-filaments in skinned fibers of rabbit skeletal-muscle. Biophys J 69 (3):1000–1010.
22. Isambert H et al (1995) Flexibility of actin-filaments derived from thermal fluctuations-effect of bound nucleotide, phalloidin, and muscle regulatory proteins. J Biol Chem 270(19):11437–11444.
23. Gittes F et al (1993) Flexural rigidity of microtubules and actin-filaments measured from thermal fluctuations in shape. J Cell Biol 120(4):923–934.
24. Tsuda Y et al (1996) Torsional rigidity of single actin filaments and actin-actin bond breaking force under torsion measured directly by in vitro micromanipulation. P Natl Acad Sci USA 93(23):12937–12942.
25. Yasuda R, Miyata H, Kinosita K (1996) Direct measurement of the torsional rigidity of single actin filaments. J Mol Biol 263(2):227–236.
26. Holmes KC et al (1990) Atomic model of the actin filament. Nature 347(6288):44–49.
27. Pollard TD (1986) Rate constants for the reactions of Atp–actin and Adp–actin with the ends of actin-filaments. J Cell Biol 103 (6):2747–2754.
28. Bell GI (1978) Models for specific adhesion of cells to cells. Science 200(4342):618–627.
29. Damköhler G (1939) Stromungs und warmeubergangsprobleme in chemischer technik and forschung. Chem Ing Tech 12:469.
30. Forgacs G (1995) On the possible role of cytoskeletal filamentous networks in intracellular signaling—an approach based on percolation. J Cell Sci 108:2131–2143.
31. Nakayama T, Yakubo K, Orbach RL (1994) Dynamical properties of fractal networks-scaling, numerical simulations, and physical realizations. Rev Mod Phys 66(2):381–443.
32. Head DA, Levine AJ, MacKintosh EC (2003) Deformation of cross-linked semiflexible polymer networks. Phys Rev Lett 91(10): 108102-1–108102-4.
33. Head DA, Levine AJ, MacKintosh FC (2003) Distinct regimes of elastic response and deformation modes of cross-linked cytoskeletal and semiflexible polymer networks. Phys Rev E 68(6): 061907-1–061907-15.
34. Volkmann N, et al (2001) An atomic model of actin filaments cross-linked by fimbrin and its implications for bundle assembly and function. J Cell Biol 153(5):947–956.
35. Wagner B, et al (2006) Cytoskeletal polymer networks: The molecular structure of cross-linkers determines macroscopic properties. P Natl Acad Sci USA 103(38):13974–13978.
36. Claessens MMAE, et al (2006) Actin-binding proteins sensitively mediate F-actin bundle stiffness. Nat Mater 5(9):748–753.
37. Dalhaimer P, Discher DE, Lubensky TC (2007) Crosslinked actin networks show liquid crystal elastomer behaviour, including soft-mode elasticity. Nat Phys 3(5):354–360.
38. Tseng Y, et al (2004) The bimodal role of filamin in controlling the architecture and mechanics of F-actin networks. J Biol Chem 279(3):1819–1826.
39. Costa KD, Hucker WJ, Yin FCP (2002) Buckling of actin stress fibers: A new wrinkle in the cytoskeletal tapestry. Cell Motil Cytoskel 52(4):266–274.
40. Pender N, Mcculloch CAG (1991) Quantitation of actin polymerization in 2 human fibroblast subtypes responding to mechanical stretching. J Cell Sci 100:187–193.
41. Yap B, Kamm RD (2005) Mechanical deformation of neutrophils into narrow channels induces pseudopod projection and changes in biomechanical properties. J Appl Physiol 98(5):1930–1939.
42. Trepat X, et al (2007) Universal physical responses to stretch in the living cell. Nature 447(7144):592–595.
43. Dhont JKG, Briels WJ (2003) Inhomogeneous suspensions of rigid rods in flow. J Chem Phys 118(3):1466–1478.
44. Belagyi J, Grof P (1983) Rotational motion of actin monomer at low and high salt concentration. Eur J Biochem 130(2):353–358.
45. Oda T, et al (1998) Effect of the length and effective diameter of F-actin on the filament orientation in liquid crystalline sols measured by X-ray fiber diffraction. Biophys J 75(6):2672–2681.
46. Isambert H, Maggs AC (1996) Dynamics and rheology of actin solutions. Macromolecules 29(3):1036–1040.
47. Humphrey W, Dalke A, Schulten K (1996) VMD: Visual molecular dynamics. J Mol Graph 14(1):33–38.